Please do not adjust margins

ARTICLE

Surface Diels-Alder adducts on multilayer graphene for the generation of edge-enriched single-atom FeN_4 sites for ORR and OER electrocatalysis†

Received 00th January 20xx,
Accepted 00th January 20xx

DOI: 10.1039/x0xx00000x

Juan Amaro-Gahete,‡[a] José A. Salatti-Dorado,‡[b] Almudena Benítez,*[c] Dolores Esquivel,[a] Valentín García-Caballero,[b] Miguel López-Haro,[d] Juan J. Delgado,[d] Manuel Cano,*[b] Juan J. Giner-Casares[b] and Francisco J. Romero-Salguero*[a]

The assembly of atomically dispersed iron-nitrogen (FeN_4) sites into graphitic structures is a promising approach for sustainable production of bifunctional electrocatalysts for oxygen electroreduction (ORR) and oxygen evolution (OER) reactions. In addition, single-atom FeN_4 sites at the edges of carbon substrates provide higher electrocatalytic performance than those in plane. Unfortunately, the conventional high-temperature pyrolysis method does not allow the generation of edge-enriched FeN_4 single-atom sites. Herein, a novel low-temperature and solvent-free mechanochemical synthesis based on the use of dipyridylpyridazine (dppz) functionalized multilayer graphene as starting material is proposed for precisely engineered location of these FeN_4 active sites at the edges. After carefully characterization of these dppz-based materials, the ORR and OER electrocatalytic performance was investigated, demonstrating the efficient formation of FeN_4 sites at the edges as well as their excellent bifunctional behavior for ORR and OER. This work paves the way for the development of sustainable approaches for the generation of edge-enriched FeN_4 single atom sites on multilayer graphene structures.

Introduction

The growing demand for renewable, clean and sustainable energy to counteract the depletion of fossil fuels and reduce CO_2 emissions as well as mitigate global warming has led the scientific community to focus great attention on the development of low-cost and efficient alternative energy resources and energy storage systems. The plenty of hydrogen in the universe and its relatively easy H_2 gas production from water by electrolysis makes it an ideal energy carrier. However, the use of the electricity from renewable energy sources (such as solar or wind power) to split water into hydrogen, which is subsequently employed in fuel cells, requires the development of efficient and low-cost electrocatalyst materials.[1-3] For these reasons, the design of non-noble-metal or metal-free catalysts showing enhanced performance towards the critical reactions involved in these electrocatalytic processes is crucial for the rapid advance of the hydrogen economy.[4,5] In this sense, highly-active bifunctional electrocatalysts for the oxygen reduction reaction (ORR) and the oxygen evolution reaction (OER) are of increasing interest due to their extensive applicability in a wide variety of renewable energy technologies such as rechargeable metal-air batteries, water splitting or reversible fuel cells.[6–10] To date, Pt- and Ru/Ir-based catalysts are generally regarded as the benchmarked commercial catalysts for ORR and OER reactions, respectively appropriate.[11]

Carbon-based electrocatalysts are promising materials for the above mentioned electrocatalytic processes, due to their good stability, high surface area, excellent electrical conductivity, and flexibility for the introduction of dopants.[12,13] Accordingly, a hot topic in electrocatalysis is focused on the appropriate doping of carbon-based materials with heteroatoms (e.g. N, S, P) and transition metals (e.g. Fe or Co) to obtain optimal electronic and geometric structures.[14–21] More concretely, density functional theory (DFT) calculations suggested that co-doping of Fe and N in the form of possible FeN_4 sites on a graphitic substrate could be as active as Pt for O_2 adsorption and subsequent O=O bond breaking during the ORR.[22–25] In this sense, nitrogen-containing functional groups on graphitic matrix also play a fundamental role in the performance and electronic conductivity of electrocatalytic processes.[26-28] Indeed, the pyridinic-N enhances the potential onset while the graphitic-N greatly improves the limiting current density for ORR in N-doped graphene and N-

[a.] Departamento Química Orgánica. Instituto de Química Fina y Nanoquímica, Universidad de Córdoba (IUNAN-UCO). Campus Universitario de Rabanales, Carretera N-IV, Ed. Marie Curie, 14071 Córdoba (Spain). E-mail: qo2rosaf@uco.es
[b.] Departamento Química Física y Termodinámica Aplicada. IUNAN-UCO. Campus Universitario de Rabanales, Carretera N-IV, Ed. Marie Curie, 14071 Córdoba (Spain). E-mail: q82calum@uco.es
[c.] Departamento Química Inorgánica e Ingeniería Química. IUNAN-UCO. Campus Universitario de Rabanales, Carretera N-IV, Ed. Marie Curie, 14071 Córdoba (Spain). E-mail: g62betoa@uco.es
[d.] Departamento de Ciencia de los Materiales e Ingeniería Metalúrgica y Química Inorgánica, Facultad de Ciencias, Universidad de Cádiz, Cádiz, Spain; Instituto de Microscopía Electrónica y Materiales (IMEYMAT), Facultad de Ciencias, Universidad de Cádiz, Cádiz, Spain.
‡ These authors contributed equally to this work.
†Electronic Supplementary Information (ESI) available: [details of any supplementary information available should be included here]. See DOI: 10.1039/x0xx00000x

Please do not adjust margins

Please do not adjust margins

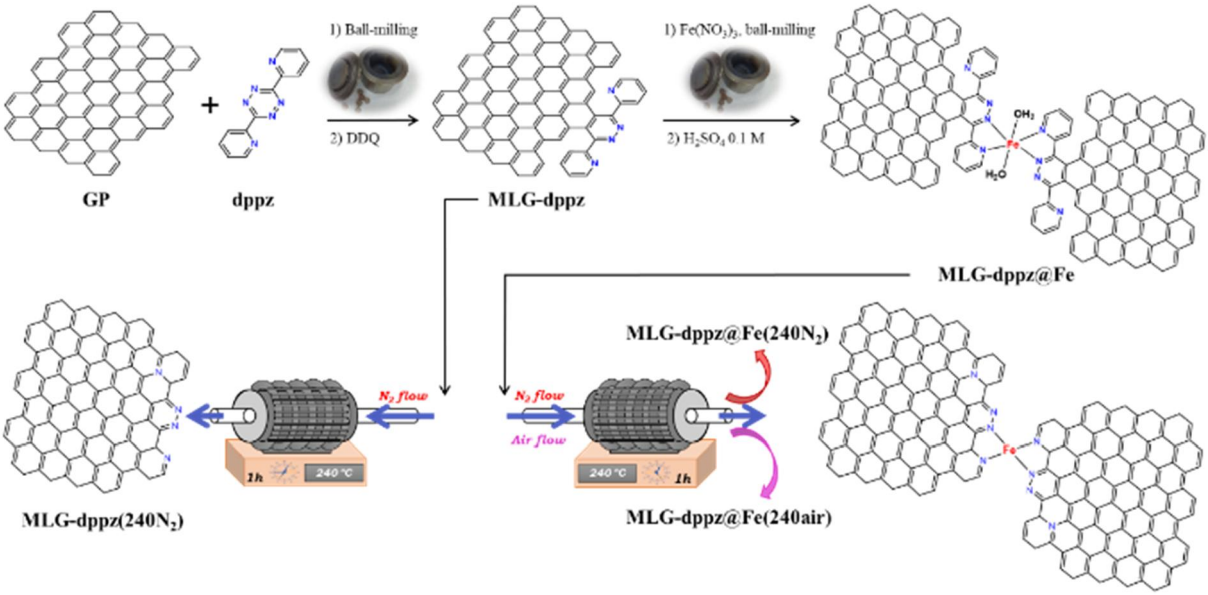

Fig. 1 Schematic diagram for the synthetic route for the preparation of MLG-dppz materials and tentative structures.

doped carbon materials.[29,30] Furthermore, the pyridinic-N species are responsible for coordinating Fe atoms to generate an FeN_4 bridging structure which, together with the synergistic effect of the graphitic-N active sites, contributes to improve the ORR electrocatalytic activity.[31–35] On the other hand, DFT calculations have confirmed that graphitic-N species created on N-doped graphene showed a low overpotential and were identified as the optimal active sites for OER electrocatalytic reactions,[36] while the reactivity of the coordinated FeN_4 species in carbon-based structures contributes positively by reducing potential barriers and improving the electrocatalytic OER activity.[37] In principle, high-performance Fe–N/C electrocatalysts should be designed by arranging N and Fe atoms to form optimal FeN_4 sites uniformly dispersed into graphitic structure.[38–43]

The preparation of this type of carbon-based materials is mainly based on two different strategies: the template-sacrifice method through metal-organic frameworks[44–49] and silica support[50–53] or the built-in FeN_4 active sites on a carbon matrix such as carbon nanotube, graphene or activated carbon.[54–58] Generally, all of these studies have reported that N-containing carbon materials can be prepared by doping with the use of ammonia, amines or N-containing organic compounds carrying out these processes by simultaneously heat-treating of an iron salt, a nitrogen precursor and a carbon support at high temperature. Consequently, the resulting types of N-sites present in those materials are mostly unpredictable and are characterized a posteriori using different techniques.

In addition, Liu and co-workers suggested in a computational study that the local carbon structure surrounding FeN_4 moiety plays a key role in determining the final catalytic properties, with FeN_4 located at the edge superior to the one in plane.[59] These results were confirmed experimentally by Xiao et al., who used a self-sacrificed templating approach to obtain enriched-edge FeN_4 sites onto graphitic nanosheets.[60] Herein, we report a novel strategy based on the use of a dipyridylpyridazine (dppz) functionalized multilayer graphene as starting material for the preparation of carbon derivatives bearing N and edge-enriched FeN4 sites, employing low-temperature and solvent-free mechanochemical synthesis method. The dppz motifs at the edge of the carbon structure exhibit a rich coordination chemistry and are capable of coordinating a great variety of metal ions due to their similarity to bipyridine-like ligands.[61–65] The synthesized materials by this method have been characterized and applied as bifunctional oxygen electrocatalysts for ORR and OER reactions.

Results and discussion

In a previous study, we reported a ball-milling synthetic procedure (i.e. a mechanochemical synthesis method) starting with graphite powder and 3,6-di(2-pyridyl)-1,2,4,5-tetrazine to produce a dipyridylpyridazine derived multilayer graphene, MLG-dppz.[61] This synthetic process involved a Diels-Alder cycloaddition between such tetrazine as an electron-deficient diene and the carbon-carbon double bonds on the edges of the graphene sheets as dienophiles. The initial adduct underwent a retro-Diels-Alder reaction with release of N_2, thus resulting in a dihydropyridazine adduct that is subsequently dehydrogenated to the corresponding pyridazine by the action of the oxidizing agent 2,3-dichloro-5,6-dicyanobenzoquinone (DDQ). The dipyridylpyridazine adducts on the edges of the graphene sheets can act as ligands for the coordination of metals. Coordinated iron sites have received much attention in recent years due to their applicability as catalysts in the energy field in substitution of expensive noble metal catalysts, mainly consisting of platinum.[66–69] Accordingly, Fe(III) nitrate was contacted with MLG-dppz to produce MLG-dppz@Fe, whose structure is tentatively proposed in **Fig. 1** by analogy to iron-bipyridine complexes, which have been used for the activation of dioxygen to oxygenate unsaturated hydrocarbons.[70,71] Thermal treatment of MLG-dppz@Fe at 240°C under a nitrogen

 This journal is © The Royal Society of Chemistry 20xx

Please do not adjust margins

Please do not adjust margins

or air atmosphere gave MLG-dppz@Fe(240N_2) and MLG-dppz@Fe(240air), respectively, whose structures are also represented in **Fig. 1**. Under these conditions, the formation of N-quaternary and tetracoordinated iron sites occurs in the graphene sheets (vide infra). The MLG-dppz material subjected to heat treatment at 240°C under nitrogen atmosphere, and so without Fe atoms, MLG-dppz(240N_2), was synthesized as a reference material to analyse the structural changes that take place in the different steps of the synthetic route.

TGA analyzes were performed for MLG-dppz and MLG-dppz@Fe confirming the thermal stability of these materials at temperatures above 240 °C (**Fig. S1**). XRD spectra of the sample MLG-dppz@Fe(240N_2) exhibited the same diffraction pattern as the starting graphite powder (**Fig. S2**) showing a strong peak at ca. 26.5°, which corresponds to the (002) graphite reflection plane and four weak peaks over 42.0°, 43.5°, 54.5° and 77.0°, attributed to the (100), (101), (004) and (110) reflections.[72–75] However, the intensity of the peak corresponding to the (002) plane decreased significantly for MLG-dppz@Fe(240N_2) compared to the pristine graphite powder, denoting exfoliation of the starting graphite to multilayer graphene.[76] The multilayered structure composed of numerous individual graphene sheets was corroborated by TEM images at different magnifications (**Fig. S3**), confirming the effectiveness of the mechanochemical synthesis process to obtain multilayer graphene with sheet average size of approximately 200 nm.[61,77,78]

Elemental analysis of the five samples gave the C, H and N contents while the amount of Fe incorporated in these materials was quantified by Inductively Coupled Plasma Mass Spectrometry (ICP-MS) (**Table 1**). The N content ranged between 1.3 and 2.2 wt.% whereas the Fe content was ca. 0.7 wt.%. Thus, the N/Fe molar ratio was ca. 8 in materials MLG-dppz@Fe, MLG-dppz@Fe(240N_2) and MLG-dppz@Fe(240air), in accordance with the coordination of one Fe atom to two dipyridylpyridazine units at the edges of two different graphene sheets forming FeN_4-like sites, as represented in **Fig. 1**.

Table 1 Elemental composition of synthesized MLG-dppz materials and N/Fe molar ratio.

Sample reference	wt.% C	wt.% H	wt.% N	wt.% Fe	N/Fe molar ratio
MLG-dppz	81.97	0.19	2.18	-	-
MLG-dppz@Fe	87.31	0.24	1.61	0.76	8.4
MLG-dppz(240N_2)	87.85	0.15	1.85	-	-
MLG-dppz@Fe(240N_2)	89.45	0.20	1.48	0.73	8.1
MLG-dppz@Fe(240air)	86.83	0.19	1.35	0.69	7.8

The surface area and pore structure of graphene-based materials play a significant role in the electrochemical behaviour for ORR and OER reactions.[14,79,80] Thus, N_2 adsorption/desorption isotherms of all materials were measured (**Fig. S4**). All isotherms exhibited a hysteresis loop characteristic of type IV isotherms in the Brunauer-Deming-Deming-Teller (BDDT) classification, which is typical of mesoporous solids. The pore size distribution analyzed by the DFT model is shown in **Fig. S5**. As observed, the thermal treatment favored the appearance of micropores. Specifically, it has been reported to be beneficial for the isolation of FeN_4 sites by preventing aggregation phenomena.[81] Brunauer-Emmett-Teller (BET) surface area, pore volume and pore diameter are given in **Table S1**. These data demonstrated that the incorporation of Fe atoms in the graphene structure promoted an increase in surface area (ca. 100 $m^2 \cdot g^{-1}$) and pore volume (ca. 0.2 $cm^3 \cdot g^{-1}$),[82] as a result of the porous structure generated by formation of FeN_4 sites, as observed by SEM microscopy (**Fig. S6**).[83] A high specific surface area provides more exposed active sites to promote electrocatalytic processes, while abundant mesopores together with a slight contribution of micropores favor the penetration of electrolytes to the catalytic centers and the effective mass transfer of the reaction intermediates.[84]

Raman spectroscopy was carried out to obtain further structural information of these materials, allowing to analyze the degree of graphitization. **Fig. 2** shows typical Raman spectra of graphitic materials highlighting two main bands centered at 1350 cm^{-1} and 1580 cm^{-1} that are commonly referred to as D-band and G-band. The D-band is attributed to the disorder degree of graphite-based materials promoted by several factors such as structural defects on the graphene sheets, the discontinuity at the edges of the graphitic planes and the functionalization reactions on the sp^2 carbon bonds. Instead, G-

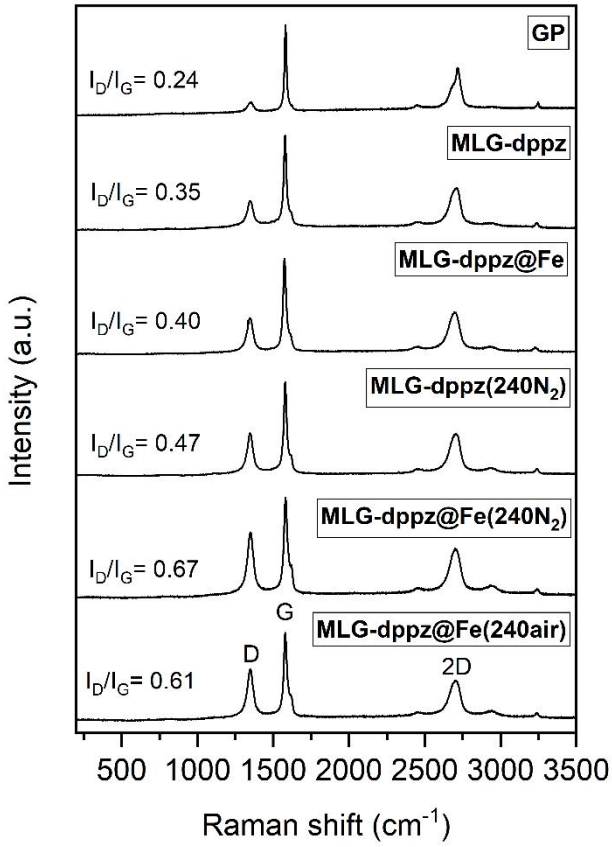

Fig. 2 Raman spectra of the different materials.

Please do not adjust margins

Please do not adjust margins

band corresponds to the first-order Raman scattering of E_{2g} phonon mode in the Brillouin zone for sp^2 hybrid carbon atoms and represents the degree of crystallinity for materials with graphitic structure.[74,85,86] Accordingly, the relative intensity ratio of the D and G peaks (I_D/I_G) provides a quantitative analysis of the structural disorder of these materials, revealing the structural changes that have taken place in each of the synthesis steps. The I_D/I_G values increased from 0.24 for the starting graphite to 0.35 for the MLG-dppz material functionalized by the Diels-Alder reaction. Following the procedure reported by J. N. Coleman et al. to measure flake thickness of exfoliated graphene by Raman spectroscopy based on the shape and intensity of the 2D band,[87] the number of sheets in MLG-dppz was 8. Accordingly, this material can be classified as multilayer graphene according to the nomenclature proposed by R. H. Hurt.[88] The incorporation of Fe atoms (MLG-dppz@Fe) or the thermal treatment (MLG-dppz(240N_2)) increased the degree of structural disorder with I_D/I_G values of 0.40 and 0.47, respectively. The level of defects in the graphitic structure was more accentuated in those materials with coordinated Fe subjected to a subsequent thermal treatment at 240 °C. The highest I_D/I_G ratio value of 0.67 was obtained for MLG-dppz@Fe(240N_2). Therefore, this material has a greater number of defects that are considered potentially conducive to promoting crucial mass transfer phenomena in the ORR electrocatalytic process.[84,89] Additionally, the exposure of more edged planes and thus more nitrogen binding sites that result in the formation of more FeN_4 sites suggests a potential improvement of its ORR electrocatalytic performance.[85,90] This argument is corroborated by elemental analysis, which accounted for a higher content of N and Fe in MLG-dppz@Fe(240N_2) than in MLG-dppz@Fe(240air).

The evolution of the chemical changes produced in the different stages of the synthetic route was analyzed by X-ray photoelectron spectroscopy (XPS). C1s high-resolution XPS spectra of the different materials were deconvoluted into six components (**Fig. S7**). The contributions and binding energies of each component used in the fitting of the C1s photoemission peak are given in **Table S2**. All materials gave similar contributions. The main one (ca. 70%) corresponded to C=C (sp^2 centers) and C-C (sp^3 centers) bonds, whose deconvoluted peak was fitted to the adventitious carbon signal at 284.8 eV. The contribution at 285.8 eV was assigned to C-N bonds (ca. 11%), mainly from pyridinic and N-graphitic species. The carbon-oxygen functional groups had a lower contribution and appeared at higher binding energies, i.e. 286.7, 287.8 and 289.1 eV associated with C-O (ca. 7%), C=O (ca. 5%) and O-C=O (ca. 4%) groups, respectively. The contribution at 291.0 eV was assigned to satellite π-π* transitions (ca. 3.5%).

Several studies have reported that the formation of FeN_4 active site bridging structures linked through two adjacent graphitic sheets is feasible at high temperature mainly due to the presence of pyridine and graphitic (quaternary) nitrogen heteroatoms.[90,91] The HR-XPS spectra of N1s (**Fig. 3**) provided the detailed analysis of the structural nitrogen evolution for each material. The N1s signal of MLG-dppz was fitted into three components. The main contribution centered at 399.2 eV was

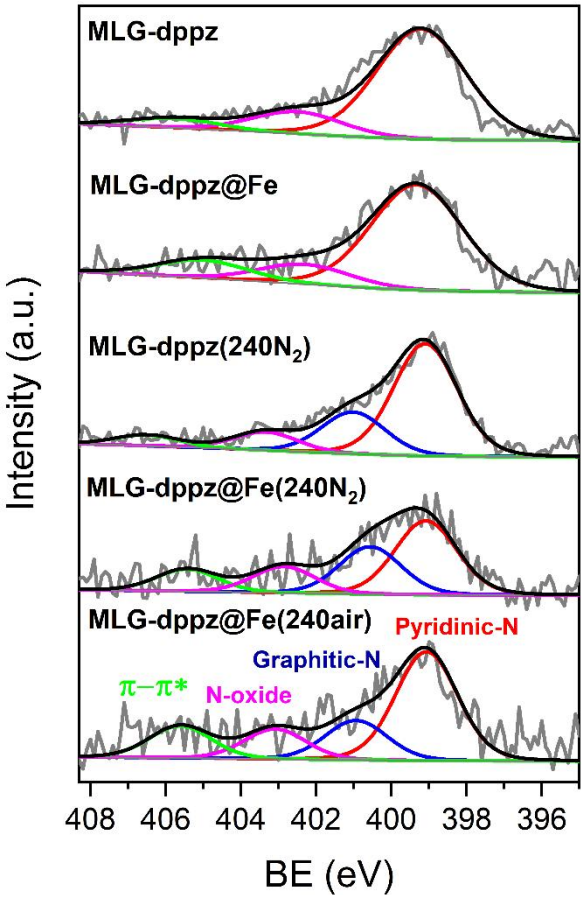

Fig. 3 N1s HR-XPS spectra of the different materials.

assigned to N in the pyridine and pyridazine rings because both contributions show the same signal after Diels-Alder reaction between graphite and dptz, in agreement with previous studies.[61,92] The two remaining lower intensity decomposed bands were assigned to N-oxide groups (402.5 eV) and π-π* transitions (405.7 eV) from aromatic rings and unsaturated bonds.[93,94] The coordination of Fe atoms in MLG-dppz@Fe did not produce any significant change in the N1s signal. Nevertheless, the thermal treatment at 240 °C undergone by samples MLG-dppz(240N_2), MLG-dppz@Fe(240N_2) and MLG-dppz@Fe(240air) led to a new component in the N1s signal at ca. 401.0 eV, which can be assigned to graphitic-N (quaternary-N).[95] This graphitic-N must be generated by an oxidative cyclodehydrogenation promoted by heating (**Fig. 1**). The contribution of each component to the N1s signal is given in **Table 2**. The pyridinic to graphitic N ratio was 2.7 for both MLG-dppz(240N_2) and MLG-dppz@Fe(240air) whereas it was 1.5 for MLG-dppz@Fe(240N_2). A high content of pyridinic-N and graphitic-N is considered a key factor to improve the ORR and OER electrocatalytic performance.[37,96,97] Accordingly, MLG-dppz@Fe(240N_2), which has the highest content of graphitic-N and iron atoms as well as a large contribution of pyridinic-N (**Table 2**), could be a promising bifunctional catalyst in ORR and OER applications. MLG-dppz@Fe(240air) will be useful to analyze the slight increase in pyridinic-N and the lower graphitic-N contribution and iron percentage.

This journal is © The Royal Society of Chemistry 20xx

Please do not adjust margins

Please do not adjust margins

Table 2 Contribution of the four components used in the fitting of the N1s photoemission peak.

N1s	*MLG-dppz*		*MLG-dppz@Fe*		*MLG-dppz(240N$_2$)*		*MLG-dppz@Fe(240N$_2$)*		*MLG-dppz@Fe(240air)*	
Surface groups	**BE (eV)**	**Atom %**	**BE (eV)**	**Atom %**	**BE (eV)**	**Atom %**	**BE (eV)**	**Atom %**	**BE (eV)**	**Atom %**
Pyridinic-N	399.2	77.8	399.3	77.2	399.1	61.3	399.1	43.5	399.1	51.7
Graphitic-N	-	-	-	-	401.0	22.8	400.6	28.0	400.9	18.8
N-oxide	402.5	15.6	402.3	13.9	403.3	10.0	402.9	15.5	403.1	14.3
π-π*	405.7	6.6	405.0	12.5	406.5	5.9	405.4	13.1	405.6	15.3

The HR-XPS Fe2p spectra are shown in **Fig. 4**. The core-level Fe2p XPS spectra of MLG-dppz@Fe was deconvoluted into three peaks: Fe2p$_{3/2}$ and Fe2p$_{1/2}$ regions at 712.5 eV and 725.8 eV, respectively, assigned to Fe(III) formal oxidation state, and the characteristic Fe^{3+} 2p$_{3/2}$ satellite peak centered at 719.1 eV, in agreement with previously reported works.[98–103] Fe2p XPS spectra of MLG-dppz@Fe(240N$_2$) and MLG-dppz@Fe(240air) were fitted into five characteristic contributions (Fe^{2+} 2p$_{3/2}$, Fe^{3+} 2p$_{3/2}$, satellite peak, Fe^{2+} 2p$_{1/2}$, Fe^{3+} 2p$_{1/2}$). The generation of Fe^{2+} species and the binding energies at ca. 711 and 715 eV, respectively, for the Fe^{2+} 2p$_{3/2}$ and Fe^{3+} 2p$_{3/2}$ signals, similar to those reported in the literature, confirmed the formation of

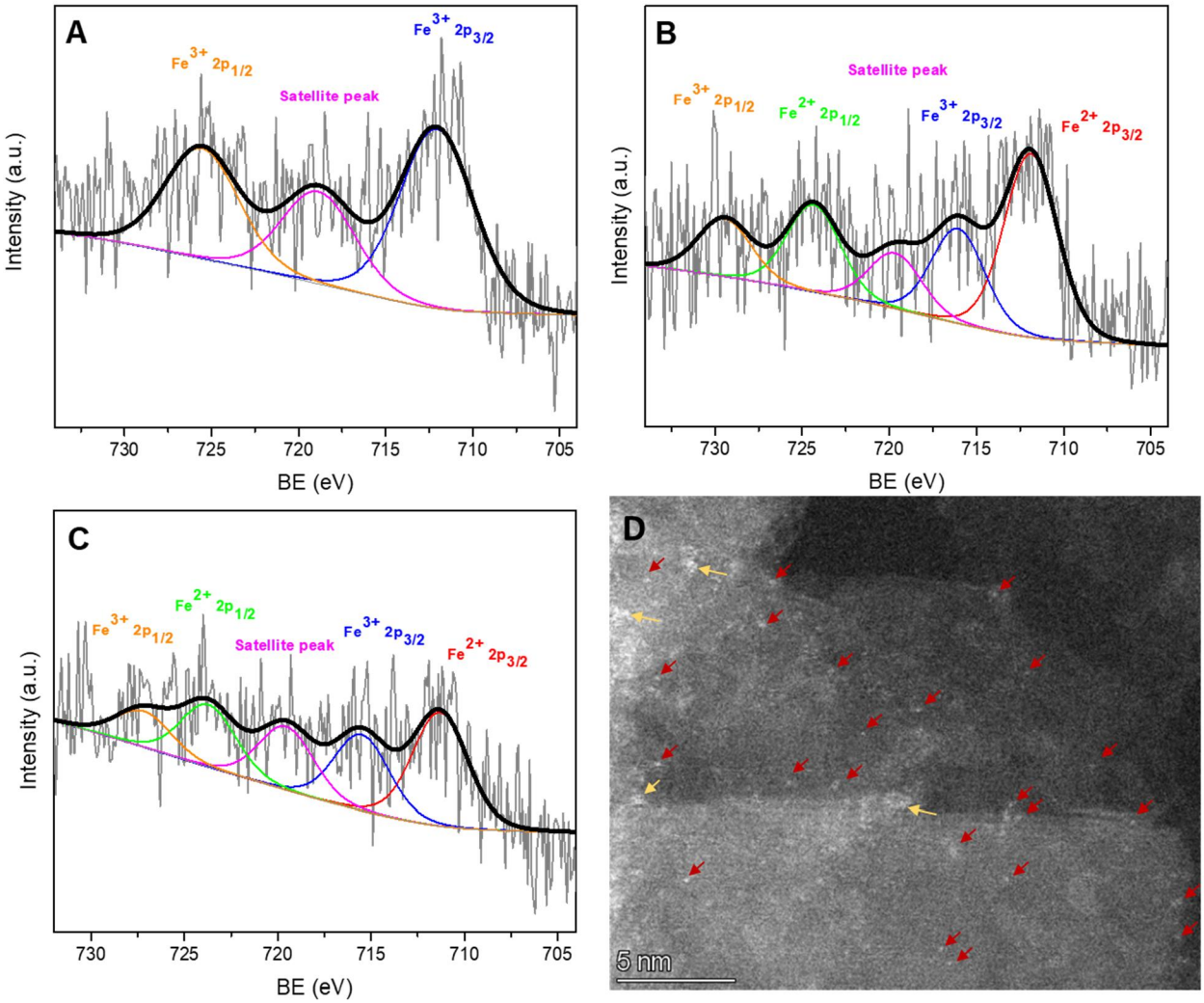

Fig. 4 Fe 2p HR-XPS spectra of (A) MLG-dppz@Fe, (B) MLG-dppz@Fe(240N$_2$) and (C) MLG-dppz@Fe(240air). (D) Aberration corrected HAADF-STEM image of sample in (B).

Please do not adjust margins

Please do not adjust margins

FeN_4 sites in these materials.[84,104,105] Clearly, the generation of reduced Fe^{2+} species was a consequence of the heat treatment at 240 °C.[106] The Fe^{2+}/Fe^{3+} ratio was 1.8 and 1.6 for MLG-dppz@Fe(240N_2) and MLG-dppz@Fe(240air), respectively. The lower fraction of Fe^{2+} in the latter can be explained by the use of an oxidizing atmosphere during the heat treatment. In fact, $FeCl_3$-mediated oxidative cyclodehydrogenation reactions under an inert atmosphere have been reported in the literature for the generation of 6N-doped nanographenes through [2+2+2] cyclotrimerisation routes.[107] Thus, the presence of Fe^{3+} ions under a nitrogen atmosphere promoted the cyclodehydrogenation reaction in MLG-dppz@Fe(240N_2), for which the lowest pyridinic to graphitic-N ratio was observed.

After exhaustive characterization, the electrocatalytic properties for ORR of the different samples were compared (**Fig. 5**). **Fig. 5A** compares the resulting electrocatalytic performance toward the ORR, reflecting the most effective mechanochemical synthesis route for the incorporation of FeN_4 sites into the graphitic structures. Overall, the maximum current density increased when the heating step at 240 °C was included during the synthesis because electrocatalytically active graphitic-N species were generated. Additionally, the current density increase was even larger when the heat treatment was carried out under inert atmosphere (a maximum current density value of -0.83 mA·cm^{-2}). These results can be explained by the presence of oxygen atmosphere during thermal treatment that favored the iron oxidation, providing a worse electrocatalytic performance. Indeed, **Fig. 5B** clearly demonstrated that the corresponding ORR cathodic peaks were not presented under a saturated N_2 environment, revealing the presence of available active Fe(II) ions related to FeN_4 coordinative structure.[108] To further demonstrate it, High resolution High Angle Annular Dark Field Scanning Transmission Electron Microscopy (HAADF-STEM) imaging was performed on MLG-dppz@Fe(240N_2). **Fig. 4D** shows a representative HAADF-STEM of this sample using spherical aberration (Cs)-corrected TEM (enlarged in **Fig. S8**). This approach allowed us to observe the presence of sub-nano clusters (yellow narrows) and even individual atoms (red narrows) of relatively heavy iron atoms on a light support such as a multilayer graphene. In addition, we can see homogeneously dispersed white dots that correspond with the iron single atoms stabilized into the FeN_4 coordinative structure. In order to confirm the chemical nature of the observed single atoms, Energy-dispersive X-ray (EDX) analysis were carried out. Due to the detection limits of the EDX detector, it was not possible to obtain a good spectrum of a single atom. For this reason, elemental mappings of large areas were recorded, and the corresponding sum spectrum was obtained. **Fig. S9** includes a representative EDX spectrum, showing the presence of low contents of both nitrogen and iron, even though in the low magnification HAADF image where it can't be observed the presence of iron nanoparticles.

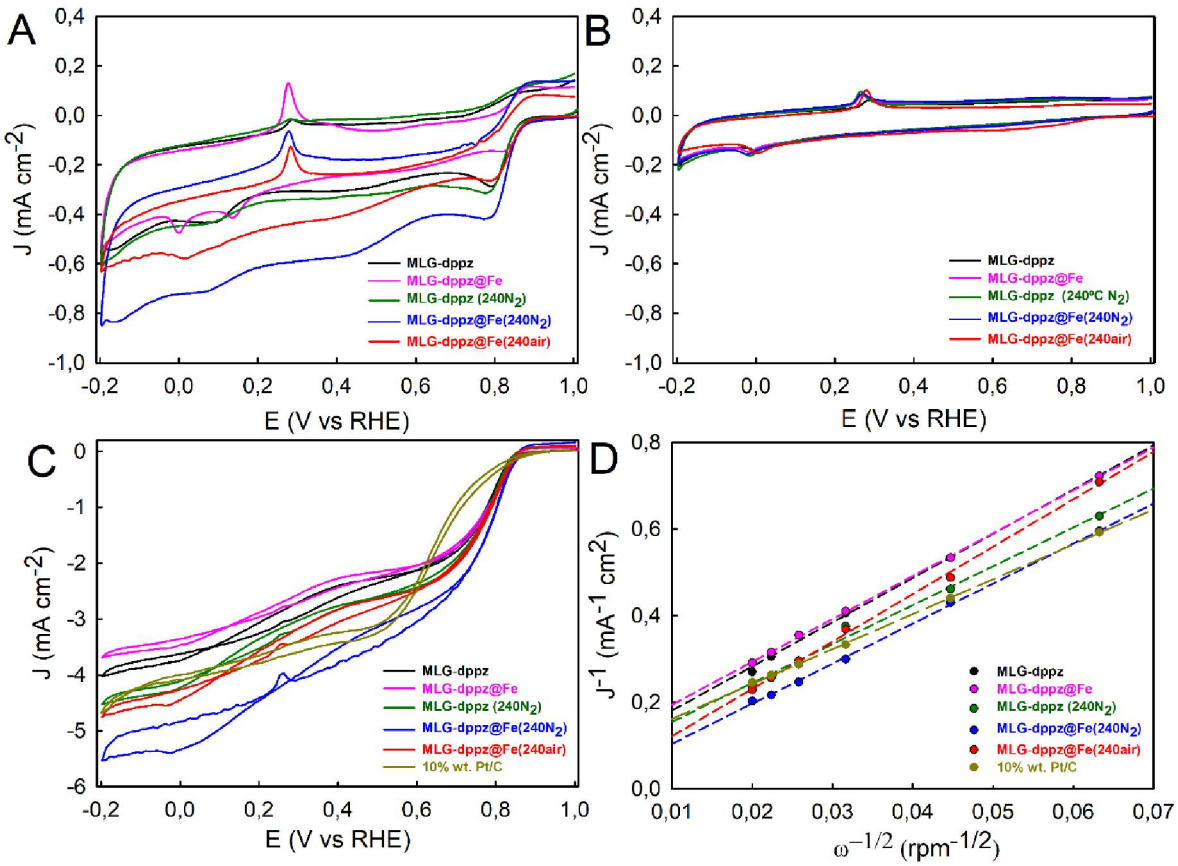

Fig. 5 CV curves obtained for the different synthesized MLG-dppz samples in O_2-saturated (A) and N_2-saturated (B) with 0.5 M KOH at 0.1 V s^{-1}. (C) RDV curves of all MLG-dppz materials at the same rotating rate of 2500 rpm. Scan rate: 10 mV s^{-1}. (D) K–L plots obtained from the RDVs in **Fig. S10** at 0.0 V (vs RHE).

This journal is © The Royal Society of Chemistry 20xx

Please do not adjust margins

Please do not adjust margins

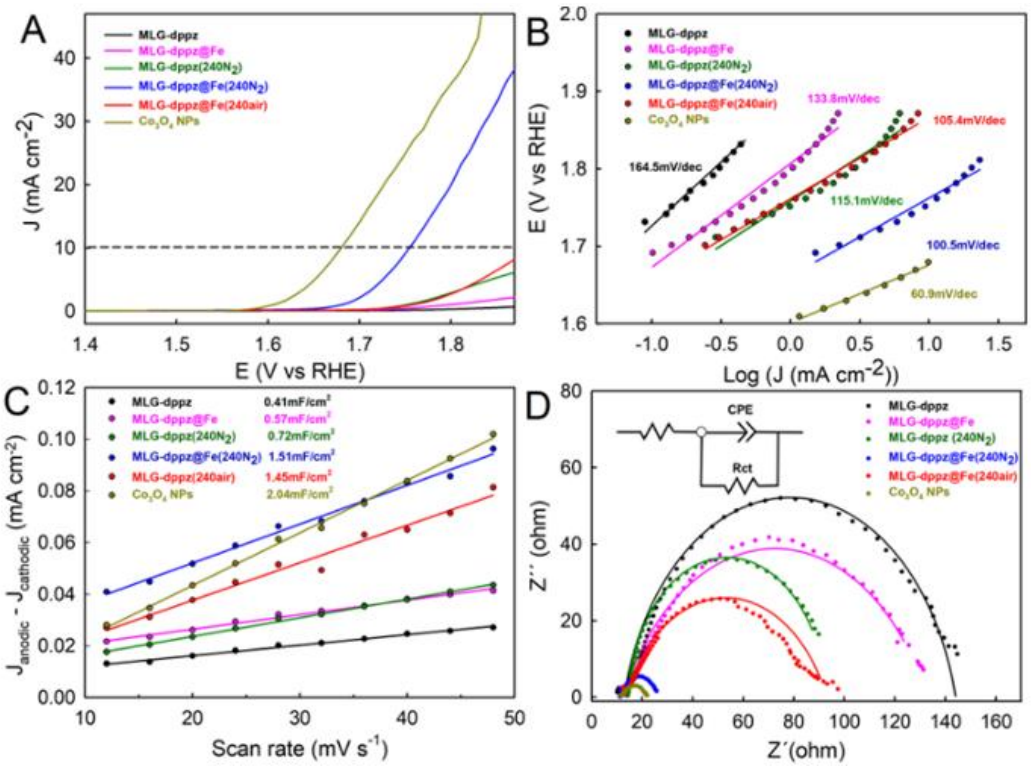

Fig. 6 (A) OER polarization curves obtained for the different MLG-dppz samples and the Co_3O_4 NPs reference material in 0.5 M KOH solution at 2 mV/s. (B) Tafel plot from (A). (C) Plots of difference of anodic and cathodic current density as a function of the scan rate, and (D) EIS curves obtained for the MLG-dppz samples at the overpotential of 700 mV, with frequency from 100 kHz to 1 Hz and amplitude of 5 mV. Dots and lines represent the experimental and simulated data, respectively.

Additionally, in order to gain further insights into the ORR, rotating-disk voltammograms (RDVs) were acquired for the different MLG-dppz derived samples in oxygen-saturated 0.5 M KOH, and at different rotation rates, ranging from 250 to 2500 rpm (**Fig. S10A-E**). As it was expected, the limiting current density in the RDVs curves increased with the increase of rotation speed due to a smaller diffusion layer at high rates, indicating a kinetics-controlled process. **Fig. 5C** compares the resulting RDV curves for the five analyzed MLG-dppz derived materials with the reference 10 % wt. Pt/C at the same rotation rate of 2500 rpm. The half-wave potentials ($E_{1/2}$) were calculated from the maxima of the derivative plots of the ORR curves shown in **Fig. 5C** (**Fig. S11**).[109] The $E_{1/2}$ values obtained for MLG-dppz, MLG-dppz@Fe, MLG-dppz(240N_2), MLG-dppz@Fe(240N_2) and MLG-dppz@Fe(240air) were 0.762, 0.810, 0.800, 0.812 and 0.802 V, respectively. The best $E_{1/2}$ value was obtained with MLG-dppz@Fe(240N_2) sample, being a better value than the reported in the literature for Pt/C (20 % wt. Pt, ca. 0.80 V).[110] In summary, the MLG-dppz@Fe(240N_2) material provided the best electrocatalytic performance with an onset potential of 0.89 V vs RHE and a maximum current density of -5.5 mA·cm^{-2} at 0.0 V vs RHE, which were better than those for Pt/C reference catalyst (i. e. 0.81 V vs RHE and -4.2 mA·cm^{-2}) and similar to the best reported ORR catalysts (**Table S3**). It should be noted that, in all cases, a hysteresis effect associated to the removal of adsorbed OH species and subsequent O_2 chemisorption from the free active sites at the metal surface can be observed, suggesting a similar reaction mechanism. **Fig. 5D** shows the resulting K-L plots for the different MLG-dppz derived samples at 0.0 V (vs RHE), demonstrating first-order reaction kinetics toward dissolved oxygen due to the excellent linearity of the experimental points.

Table 3 ORR kinetic parameters for ORR of the different synthesized MLG-dppz materials obtained from Fig. 5C and 5D.

Paramet.	*MLG-dppz*	*MLG-dppz@Fe*	*MLG-dppz (240N_2)*	*MLG-dppz@Fe (240N_2)*	*MLG-dppz@Fe (240air)*	*10% wt. Pt/C*
E_{onset} (V)	0.872	0.889	0.892	0.892	0.892	0.810
n	3.55	3.66	4.03	3.92	3.31	4.19
J_k (mAcm^{-2})	-12.80	-10.55	-15.52	-86.59	-84.09	-12.34
K(cm s^{-1})	0.13	0.11	0.16	0.87	0.85	0.28

The resulting slope and y-intercept were used to calculate the average number of electrons transferred (n) per oxygen molecule and other ORR kinetic parameters (**Table 3**). The resulting ORR kinetics parameters (n, J_k and k) of the different synthesized materials suggested the following electrocatalytic performance order: MLG-dppz@Fe < MLG-dppz < MLG-dppz(240N_2) < MLG-dppz@Fe(240air) < MLG-dppz@Fe(240N_2). Therefore, MLG-dppz@Fe(240N_2) is the most suitable electrocatalyst for ORR, providing a four-electron pathway. These results corroborated the XPS analysis confirming the importance of the inert calcination treatment for the formation

Please do not adjust margins

Please do not adjust margins

of higher content of graphitic-N and coordinated FeN_4 active sites in the multilayer graphene structure, both carrying out a synergistic effect to promote an improved ORR activity.

The OER electrocatalytic performance for the synthesized MLG-dppz derived samples were investigated through LSV curves in 0.5 M KOH electrolyte. **Fig. 6A** shows that the resulting current density increased with the potential change for the different materials, as expected for OER anodic processes. For the evaluation of their electrocatalyst activity, the overpotentials at the geometric current density of 10 mA·cm^{-2} were measured.[111,112] As shown in **Fig. 6A**, the MLG-dppz@Fe(240N_2) showed the lowest overpotential of 500 mV at 10 mA cm^{-2}, which was similar to that of previously reported OER catalysts (**Table S4**). This overpotential was slightly higher than that of the Co_3O_4 NPs reference material (450 mV), which gave a quite similar value to that previously reported by Leal-Rodríguez et al. (430 mV),[112] thus demonstrating the excellent electrocatalytic performance of MLG-dppz@Fe(240N_2) despite its very low Fe content (0.73 %). These results can be attributed to the great availability of the highly disperse FeN_4 active centers, which significantly favored the water oxidation process. It further confirmed the most efficient route for the generation of high graphitic-N content during the calcination stage under inert atmosphere, proving to play a key role in OER processes.[36] More concretely, the MLG-dppz@Fe(240air) sample provided lower OER electrocatalytic performance than MLG-dppz(240N_2). The calcination stage at 240 °C under inert atmosphere significantly improved the OER electrocatalytic performance of MLG-dppz@Fe, partially avoiding the oxidation of Fe^{2+} to Fe^{3+} observed under oxygen-saturated conditions. These results were more evident when comparing the resulting maximum current density values (**Fig. 6A**). In addition, the Tafel slope was determined to evaluate the OER mechanism and rate-determining step (**Fig. 6B**). The resulting Tafel slope values indicated that the third reaction of the physisorbed hydrogen peroxide based-mechanism for OER in alkaline media was rate-determining step for all samples.[113,114] Overall, a lower Tafel slope is beneficial for a faster increase in the reaction rate. In this sense, a significative Tafel slope decrease can be observed with the increase of the FeN_4 active centers and graphitic-N species, confirming that the enhance of the electrocatalytic performance is associated to the inert heat treatment to produce the efficient coordination of Fe atoms into the pyridinic-N and the generation of graphitic-N into the multilayer graphene structures.

The total electrode activity was determined by the total number of active sites.[112] **Fig. 6C** plots the difference of anodic and cathodic current density against the scan rate, where the resulting slope (areal capacitance) was proportional to their ECSA. Accordingly, MLG-dppz@Fe(240N_2) showed the highest areal capacitance of 1.51 mF·cm-^{2} (2.04 mF·cm^{-2} for the reference Co_3O_4 NPs and 2.36 mF·cm^{-2} for the previously reported by Leal-Rodríguez et al.[112]). As the number of active sites favor the charge transfer, EIS analysis were conducted for the different samples (**Fig. 6D**), confirming the previous findings. The EIS results were fitted based on the equivalent circuit (**Fig. 6D**, inset), and the obtained solution resistance (Rs), charge-transfer resistance (Rct) and constant phase elements (CPE) are summarized in **Table 4**.[115] The CPE-T parameter is referred to pseudo capacitance and CPE-P is related to depressed semicircle in the EIS plot.[116] As expected, MLG-dppz@Fe(240N_2) provided the best charge transport efficiency with the smallest Rct of 15.87 Ω·cm^{-2}, while MLG-dppz showed the highest Rct of 131.00 Ω·cm^{-2}. The resulting Rct value in the former case was similar to that of the reference material Co_3O_4 NPs (12.35 Ω·cm^{-2}).

Table 4 Summary data obtained from the simulation of the equivalent circuit for the MLG-dppz samples, and the Co_3O_4 NPs used as reference material.[112]

Sample reference	Rs [Ω/cm^2]	Rct [Ω/cm^2]	CPE-T	CPE-P
MLG-dppz	12.80	131.00	5.03 x 10^{-7}	0.8556
MLG-dppz@Fe	12.44	120.19	1.74 x 10^{-5}	0.7305
MLG-dppz(240N_2)	14.34	78.55	3.77 x 10^{-4}	0.9532
MLG-dppz@Fe(240N_2)	13.73	15.87	3.98 x 10^{-4}	0.9040
MLG-dppz@Fe(240air)	13.11	79.97	1.1 x 10^{-5}	0.7331
Co_3O_4 NPs	18.20	12.35	6.5 x 10^{-4}	0.6905

Conclusions

A novel low-temperature and solvent-free mechanochemical synthesis strategy based on dppz functionalized multilayer graphene for the generation of edge-enriched FeN_4 sites was successfully developed. Our findings demonstrate that dppz adducts on the edges of the graphene sheets can act as ligands for the coordination of iron. The subsequent thermal treatment of MLG-dppz@Fe at 240 °C under a nitrogen atmosphere provided more successful incorporation of edge-enriched FeN_4 sites than that under air conditions. The resulting MLG-dppz@Fe(240N_2) material provides bifunctional electrocatalytic performance for ORR and OER. Our low-temperature synthesis with low-iron content paves the way for the development of novel sustainable approaches for the generation of edge-enriched FeN_4 single atom sites on multilayer graphene structures with bifunctional electrocatalytic properties.

Experimental

The conclusions section should come in this section at the end of the article, before the acknowledgements.

Materials

Graphite powder extra fine (GP), 2-pyridinecarbonitrile ($C_6H_4N_2$, 99%), hydrazine hydrate (reagent grade, N_2H_4 50-60 %), acetic acid (CH_3COOH, ReagentPlus, ≥99.99%), sodium nitrite ($NaNO_3$, ACS reagent, ≥97.0%), 2,3-dichloro-5,6-dicyano-p-benzoquinone (DDQ, 98%) and sulfuric acid (H_2SO_4, ACS reagent, 95.0-98.0%) were purchased from Sigma Aldrich. Iron (III) nitrate nonahydrate pure ($Fe(NO_3)_3·9H_2O$, 98%) was

This journal is © The Royal Society of Chemistry 20xx

Please do not adjust margins

Please do not adjust margins

obtained from PanReac AppliChem. Dichloromethane (CH_2Cl_2, anhydrous, ≥99.8%, contains 40-150 ppm amylene as stabilizer), chloroform ($CHCl_3$, anhydrous, ≥99%, contains 0.5-1.0% ethanol as stabilizer) and ethanol were purchased from Labbox Labware S.L. All the reagents and solvents were used as received without further purification. 3,6-Di(2-pyridyl)-1,2,4,5-tetrazine (dptz) were synthesized by a previously reported procedure.[64]

Mechanochemical-based synthesis

Synthesis of MLG-dppz. The MLG-dppz material was obtained according to the following experimental procedure, which is a modified synthesis for obtaining multilayer graphene adapted from that previously reported by Amaro et al.[61] 2 g of GP and 0.5 g of dptz (2 mmol) were introduced into a planetary ball mill (Retsch PM100, Retsch GmbH, Haan, Germany). The dry milling process was carried out at 600 rpm with reversal of rotation every 30 min during 24 h. Subsequently, the solid obtained was washed twice at room temperature and at 40 °C with 150 mL of CH_2Cl_2 to remove excess unreacted dptz and then dried at 120 °C under vacuum overnight. After that, the product was aromatized using DDQ with a solid:DDQ weight ratio of 4:1 in 150 mL of $CHCl_3$ for 24 h at room temperature. The solid was washed five times with $CHCl_3$ by successive redispersions to eliminate excess of DDQ. The resulting material, named MLG-dppz, was dried under vacuum at 120 °C overnight. Further details about the Diels-Alder reaction between 3,6-di(2-pyridyl)-1,2,4,5-tetrazine and different graphene-based materials with several activation processes and reaction times were previously reported.[61]

Synthesis of MLG-dppz@Fe. For the preparation of MLG-dppz@Fe, 2 g of MLG-dppz and excess amount of $Fe(NO_3)_3{\cdot}9H_2O$ (0.404 g, 1 mmol) were reacted by dry ball milling process (Retsch PM100, Retsch GmbH, Haan, Germany) at 600 rpm with reversal of rotation every 30 min during 24 h. After this process, the solid was washed with a 0.1 M H_2SO_4 solution to remove excess unreacted iron salt. The dispersion was filtered and then washed several times with distilled water. Finally, the material was dried at 120 °C under vacuum overnight.

Synthesis of MLG-dppz(240N$_2$). MLG-dppz (1 g) was subjected to a pyrolysis treatment in a tubular furnace (Carbolite Gero CTF, Parsons Lane, Hope Valley, UK) at 240 °C under a nitrogen atmosphere using a heating ramp of 10 °C·min^{-1} for 1 h. The pyrolyzed sample was named MLG-dppz(240N$_2$).

Synthesis of MLG-dppz@Fe(240N$_2$). MLG-dppz@Fe (0.8 g) was treated under the same heating conditions as the MLG-dppz(240N$_2$) obtaining the material MLG-dppz@Fe(240N$_2$).

Synthesis of MLG-dppz@Fe(240air). MLG-dppz@Fe (0.8 g) was subjected to a thermal treatment in a tubular furnace (Carbolite Gero CTF, Parsons Lane, Hope Valley, UK) at 240 °C under an air atmosphere using a heating ramp of 10 °C·min^{-1} for 1 h. The resulting material was named MLG-dppz@Fe(240air).

Characterization

Iron loadings in MLG-dppz@Fe based materials were quantified by ICP-MS analysis in an ICP Mass Spectrometer model NexIONTM 350X, PerkinElmer Inc. The analytical procedure was carried out dissolving 1 mg of MLG based materials in a mixture of 200 mL of 69 % HNO_3 (Merck, Suprapur), 50 mL of 30 % H_2O_2 (Fluka, TraceSELECT@Ultra), 20 mL of 40 % HF (Merck, Suprapur) and Milli-Q ultrapure water up to a total volume of 5 mL using an Ultrawave Single Reaction Chamber Microwave Digestion System, Milestone Inc. at 1500 W and temperature up to 220 °C. The nitrogen content was determined by CHNS elemental analysis in an elemental analyzer TruSpec Micro CHNS, LECO. In a typical experimental, 2 mg of material were combusted with pure oxygen at a maximum temperature of 1050 °C and the products were analyzed by means of an infrared cell (CO_2, H_2O and SO_2) or a thermal conductivity cell (N_2). The samples morphology was investigated by transmission electron microscopy (TEM) and scanning electron microscopy (SEM). TEM images were recorded on a JEOL JEM-1400 transmission electron microscope operated at an accelerating voltage of 120 kV. Samples were ultrasonically dispersed in isopropanol and subsequently deposited on holey carbon films supported on copper grids (Agar Scientific Ltd). JEOL JSM-7800F scanning electron microscope was used to obtain SEM images. X-Ray Diffraction (XRD) patterns were recorder on a BrukerD8 Discover A25 X-ray diffractometer by using filtered Cu Kα radiation within a 2θ angle range between 5° and 80° at a rate of 1.05 s per step with a step size of 0.04° in continuous mode. Thermogravimetric analysis (TGA) was performed in a Mettler Toledo TGA/DSC equipment (Mettler-Toledo, Columbus, OH, USA) under nitrogen or oxygen atmosphere, heating the samples from 30 to 900 °C at 10 °C·min^{-1}. Raman spectra were recorded in a Renishaw Raman instrument (InVia Raman Microscope) equipped with a Leica microscope and a Renishaw CCD Camera (578x400) using a green laser light excitation source (532 nm). A total of 20 scans per spectrum were acquired to improve the signal-to-noise ratio, 10 s of exposure time and laser power of 10 % over the maximum provided. Specific surface areas, pore sizes and pore volumes were examined from the N_2 adsorption–desorption isotherms with an Autosorb iQ/ASiQwin (Quantachrome Instruments, Boynton Beach, FL, USA). The samples were previously outgassed under vacuum at 120 °C overnight. X-ray photoelectron spectroscopy (XPS) was performed on a SPECS mod. PHOIBOS 150 MCD spectrometer using monochromatic Mg Kα radiation and a multichannel detector. Previously, the samples were outgassed under vacuum in an ultra-high vacuum (UHV) multipurpose surface analysis system Specs™. All spectra were fitted to Gauss–Lorentz curves to adequate identification of the different functional groups and iron oxidation states in each material. The charging effect was corrected by taking the adventitious carbon to 284.8 eV as a reference. High resolution High Angle Annular Dark Field Scanning Transmission Electron Microscopy (HAADF-STEM) imaging was performed on a double aberration corrected (AC), monochromated, FEI Titan3 Themis 60–300 microscope operated at 300 kV.

Electrocatalytic measurements

Please do not adjust margins

Please do not adjust margins

Both ORR and OER electrochemical activities of the different synthesized MLG-dppz electrocatalyst materials and its constituent components were evaluated by a Potentiostat/Galvanostat (EmStat 3, PalmSens electrochemical analyzer) using a three-electrode configuration. A graphite sheet and an Ag/AgCl electrode were used as counter and reference electrodes, respectively. Whilst a glassy carbon (GC) disk of 5 mm in diameter (Pine Instruments Company) was used as the working electrode. A water dispersion of 5 mg·mL^{-1} of sample concentration was prepared and sonicated for 15 min. Pt/C sample (10 % wt. Pt) was prepared in a similar manner (i.e. without Nafion). Then, 25 µL of the latter suspension was drop-casted onto the clean surface of the GC and was dried slowly overnight at room temperature. The ORR electrocatalytic measurements were conducted in N_2 or O_2 saturated 0.5 M KOH electrolyte, whilst the OER measurements were performed in 0.5 M KOH under air conditions. Current densities were normalized according to the geometric surface area of GC. OER potentials (vs. Ag/AgCl) were calibrated with reference to the reversible hydrogen electrode (RHE) using the Nernst equation.[66–68]

$$E_{RHE} = E_{Ag/AgCl} + 0.1976 + 0.059\ pH \quad (1)$$

ORR analyses were performed by cyclic voltammetry (CV). For this, room temperature electrochemical measurements were recorded in the potential range from 0.00 to -1.2 V (vs. Ag/AgCl) at a scan rate of 10 mV·s^{-1}, and under static or dynamic conditions. The different rotation rates used were from 250 to 2500 rpm. The ORR kinetics parameters were analyzed using Koutecky-Levich (K-L) equations:

$$\frac{1}{J} = \frac{1}{J_L} + \frac{1}{J_k} = \frac{1}{B\omega^{1/2}} + \frac{1}{J_k} \quad (2)$$

$$J_k = nFkC_0 \quad (3)$$

$$B = 0.62nFC_0D_0^{2/3}v^{-1/6} = B^*n \quad (4)$$

where J is the measured current density, J_K and J_L are the kinetic and diffusion limiting current densities, respectively, at 0.0 V vs. RHE, ω is the electrode rotation rate, n is the overall number of electrons transferred in oxygen reduction, F is the Faraday constant, C_0 is the bulk concentration of O_2 dissolved in the electrolyte (1.03·10^{-3} mol·L^{-1} for 0.5 M KOH), D_0 is the diffusion coefficient of O_2 (1.63·10^{-5} cm2·s-1 for 0.5 M KOH), v is the kinematic viscosity of the electrolyte (0.01 cm^2·s^{-1} for 0.5 M KOH), and k is the electron transfer rate constant during ORR. B* is a constant (2.76·10^{-2} A·cm^{-2}·rpm$^{-1/2}$) for all the performed experiments.[117,118]

For OER analyses, linear-sweep voltammetry (LSV) was performed. These measurements were recorded using a scan rate of 2 mV·s^{-1} and a rotation rate of 1600 rpm. Tafel slope was determined to further analyse the mechanism and kinetics of the OER rate-determining step. The analysis of the number of active sites of the different materials was inferred through the electrocatalytic surface area (ECSA), which is proportional to some previously reported cases.[112] Typically, several cyclic voltammetries (CVs) were measured in a narrow potential window of -0.717 V to -0.817 V vs. RHE (i.e., where no faradaic reactions occurred) at different scan rates, from 12 to 48 mV·s^{-1} at an interval of 4 mV·s^{-1}. Sequentially, the slope of the resulting line (areal capacitance) for plotting the scan rate (X axis) against the J anodic-J cathodic (at -0.767 V vs. RHE – Y axis) was proportional to the ECSA. In addition, electrochemical impedance spectroscopy (EIS) was performed to analyse the charge-transfer resistance (R_{ct}) of the different MLG-dppz samples, aiming to identify the synthesized material with the most efficient charge transport (i.e., lower R_{ct} value).

Conflicts of interest

There are no conflicts to declare.

Acknowledgements

The authors wish to acknowledge the financial support from Ramon Areces Foundation, Spanish Ministry of Science, Innovation and Universities for an FPU teaching and research fellowship (FPU17/03981) and Projects RTI2018-101611-B-I00, CTQ2017-83961-R (MANA), CTQ2017-92264-EXP (JEANS) and PID2020-112744GB-I00 (BIOMINA), Andalusian Regional Government (FQM-346, FQM-175 and FQM-204 groups) and Feder Funds (UCO-1263193 -PAIDI2018- and P20_01151 -PAIDI2020- projects).

Notes and references

1 J. O. Abe, A. P. I. Popoola, E. Ajenifuja, O. M. Popoola, *Int. J. Hydrogen Energy*, 2019, **44**, 15072–15086.
2 N. Sazali, *Int. J. Hydrogen Energy*, 2020, **45**, 18753–18771.
3 K. Chen, K. Liu, P. An, H. Li, Y. Lin, J. Hu, C. Jia, J. Fu, H. Li, H. Liu, Z. Lin, W. Li, J. Li, Y.-R. Lu, T.-S. Chan, N. Zhang, M. Liu, *Nat. Commun.*, 2020, **11**, 4173.
4 Y. P. Zhu, C. Guo, Y. Zheng, S.-Z. Qiao, *Acc. Chem. Res.*, 2017, **50**, 915–923.
5 M. D. Bhatt, J. Y. Lee, *Energy & Fuels*, 2020, **34**, 6634–6695.
6 Z.-F. Huang, J. Wang, Y. Peng, C.-Y. Jung, A. Fisher, X. Wang, *Adv. Energy Mater.*, 2017, **7**, 1700544.
7 H.-F. Wang, C. Tang, Q. Zhang, *Adv. Funct. Mater.*, 2018, **28**, 1803329.
8 H. Wang, M. Zhou, P. Choudhury, H. Luo, *Appl. Mater. Today*, 2019, **16**, 56–71.
9 Z. Wu, X. F. Lu, S. Zang, X. W. Lou, *Adv. Funct. Mater.*, 2020, **30**, 1910274.
10 K. Zeng, X. Zheng, C. Li, J. Yan, J. Tian, C. Jin, P. Strasser, R. Yang, *Adv. Funct. Mater.*, 2020, **30**, 2000503.
11 C. Wei, R. R. Rao, J. Peng, B. Huang, I. E. L. Stephens, M. Risch, Z. J. Xu, Y. Shao-Horn, *Adv. Mater.*, 2019, **31**, 1806296.
12 J. Zhang, Z. Xia, L. Dai, *Sci. Adv.*, 2015, **1**, e1500564.
13 C. Hu, L. Dai, Angew. Chem. Int. Ed., 2016, 55, 11736–11758.
14 J. Duan, S. Chen, M. Jaroniec, S. Z. Qiao, *ACS Catal.*, 2015, **5**, 5207–5234.
15 Z. Wu, M. Song, J. Wang, X. Liu, *Catalysts*, 2018, **8**, 196.
16 J. Oh, S. Park, D. Jang, Y. Shin, D. Lim, S. Park, *Carbon*, 2019, **145**, 481–487.
17 K. Gao, B. Wang, L. Tao, B. V. Cunning, Z. Zhang, S. Wang, R. S. Ruoff, L. Qu, *Adv. Mater.*, 2019, **31**, 1805121.
18 B. Wang, B. Liu, L. Dai, *Adv. Sustain. Syst.*, 2021, **5**, 2000134.
19 D. Wang, X. Pan, P. Yang, R. Li, H. Xu, Y. Li, F. Meng, J. Zhang, M. An, *ChemSusChem*, 2021, **14**, 33–55.

This journal is © The Royal Society of Chemistry 20xx

Please do not adjust margins

Please do not adjust margins

20 H. Yang, R. Shi, L. Shang, T. Zhang, *Small Structures*, 2021, **2**, 2100007.
21 S. Chen, T. Luo, K. Chen, Y. Lin, J. Fu, K. Liu, C. Cai, Q. Wang, H. Li, X. Li, J. Hu, H. Li, M. Zhu, M. Liu, *Angew. Chem. Int. Ed.*, 2021, **60**, 16607-16614.
22 S. Kattel, G. Wang, *J. Mater. Chem. A*, 2013, **1**, 10790–10797.
23 S. Kattel, G. Wang, *J. Phys. Chem. Lett.*, 2014, **5**, 452–456.
24 E. F. Holby, G. Wu, P. Zelenay, C. D. Taylor, *J. Phys. Chem. C*, 2014, **118**, 14388–14393.
25 W.-J. Jiang, L. Gu, L. Li, Y. Zhang, X. Zhang, L.-J. Zhang, J.-Q. Wang, J.-S. Hu, Z. Wei, L.-J. Wan, *J. Am. Chem. Soc.*, 2016, **138**, 3570–3578.
26 T. Van Khai, H. G. Na, D. S. Kwak, Y. J. Kwon, H. Ham, K. B. Shim, H. W. Kim, *J. Mater. Chem.*, 2012, **22**, 17992.
27 Y. Zhang, J. Ge, L. Wang, D. Wang, F. Ding, X. Tao, W. Chen, *Sci. Rep.*, 2013, **3**, 2771.
28 Y. Lin, K. Liu, K. Chen, Y. Xu, H. Li, J. Hu, Y.-R. Lu, T.-S. Chan, X. Qiu, J. Fu, M. Liu, *ACS Catal.*, 2021, **11**, 6304-6315.
29 L. Lai, J. R. Potts, D. Zhan, L. Wang, C. K. Poh, C. Tang, H. Gong, Z. Shen, J. Lin, R. S. Ruoff, *Energy Environ. Sci.*, 2012, **5**, 7936.
30 K. Ai, Y. Liu, C. Ruan, L. Lu, G. M. Lu, *Adv. Mater.*, 2013, **25**, 998–1003.
31 Y. Zhan, J. Huang, Z. Lin, X. Yu, D. Zeng, X. Zhang, F. Xie, W. Zhang, J. Chen, H. Meng, *Carbon*, 2015, **95**, 930–939.
32 S. Gupta, S. Zhao, O. Ogoke, Y. Lin, H. Xu, G. Wu, *ChemSusChem*, 2017, **10**, 774–785.
33 J. Zhang, J. Wang, Z. Wu, S. Wang, Y. Wu, X. Liu, *Catalysts*, 2018, **8**, 475.
34 X. Fu, N. Li, B. Ren, G. Jiang, Y. Liu, F. M. Hassan, D. Su, J. Zhu, L. Yang, Z. Bai, et al., *Adv. Energy Mater.*, 2019, **9**, 1803737.
35 H. S. Jena, C. Krishnaraj, S. Parwaiz, F. Lecoeuvre, J. Schmidt, D. Pradhan, P. Van Der Voort, *ACS Appl. Mater. Interfaces*, 2020, **12**, 44689–44699.
36 X. Kong, Q. Liu, D. Chen, G. Chen, *ChemCatChem*, 2017, **9**, 846–852.
37 C. Lei, H. Chen, J. Cao, J. Yang, M. Qiu, Y. Xia, C. Yuan, B. Yang, Z. Li, X. Zhang, et al., *Adv. Energy Mater.*, 2018, **8**, 1801912.
38 Y. Zhu, B. Zhang, D.-W. Wang, D. S. Su, *ChemSusChem*, 2015, **8**, 4016–4021.
39 Q. Jia, N. Ramaswamy, H. Hafiz, U. Tylus, K. Strickland, G. Wu, B. Barbiellini, A. Bansil, E. F. Holby, P. Zelenay, et al., *ACS Nano*, 2015, **9**, 12496–12505.
40 A. Zitolo, V. Goellner, V. Armel, M.-T. Sougrati, T. Mineva, L. Stievano, E. Fonda, F. Jaouen, *Nat. Mater.*, 2015, **14**, 937–942.
41 M. J. Workman, A. Serov, L. Tsui, P. Atanassov, K. Artyushkova, *ACS Energy Lett.*, 2017, **2**, 1489–1493.
42 N. Alonso-Vante, Y. Feng, H. Yang, *Catalysts*, 2019, **9**, 731.
43 H. Shen, T. Thomas, S. A. Rasaki, A. Saad, C. Hu, J. Wang, M. Yang, *Electrochem. Energy Rev.*, 2019, **2**, 252–276.
44 X. Wang, H. Zhang, H. Lin, S. Gupta, C. Wang, Z. Tao, H. Fu, T. Wang, J. Zheng, G. Wu, et al., *Nano Energy*, 2016, **25**, 110–119.
45 H. Zhang, S. Hwang, M. Wang, Z. Feng, S. Karakalos, L. Luo, Z. Qiao, X. Xie, C. Wang, D. Su, et al., *J. Am. Chem. Soc.*, 2017, **139**, 14143–14149.
46 X. Zhang, X. Han, Z. Jiang, J. Xu, L. Chen, Y. Xue, A. Nie, Z. Xie, Q. Kuang, L. Zheng, *Nano Energy*, 2020, **71**, 104547.
47 W. Xue, Q. Zhou, X. Cui, S. Jia, J. Zhang, Z. Lin, *Nano Energy*, 2021, **86**, 106073.
48 S. Chen, M. Cui, Z. Yin, J. Xiong, L. Mi, Y. Li, *ChemSusChem*, 2021, **14**, 73–93.
49 Q. Wang, Y. Yang, F. Sun, G. Chen, J. Wang, L. Peng, W.-T. Chen, L. Shang, J. Zhao, D. Sun-Waterhouse, T. Zhang, G. I. N. Waterhouse, *Adv. Energy Mater.*, 2021, **11**, 2100219.
50 K. Wan, G.-F. Long, M.-Y. Liu, L. Du, Z.-X. Liang, P. Tsiakaras, *Appl. Catal. B*, 2015, **165**, 566–571.
51 S.-H. Liu, S.-C. Chen, *Carbon*, 2016, **105**, 282–290.
52 R. Gokhale, Y. Chen, A. Serov, K. Artyushkova, P. Atanassov, *Electrochim. Acta*, 2017, **224**, 49–55.
53 Y. Chen, R. Gokhale, A. Serov, K. Artyushkova, P. Atanassov, *Nano Energy*, 2017, **38**, 201–209.
54 J. Yang, D.-J. Liu, N. N. Kariuki, L. X. Chen, *Chem. Commun.*, **2008**, 329–331.
55 C. Domínguez, F. J. Pérez-Alonso, M. A. Salam, S. A. Al-Thabaiti, M. A. Peña, F. J. García-García, L. Barrio, S. Rojas, *Appl. Catal. B*, 2016, **183**, 185–196.
56 Z. Li, X. Liang, Q. Gao, H. Zhang, H. Xiao, P. Xu, T. Zhang, Z. Liu, *Carbon*, 2019, **154**, 466–477.
57 N. Cai, S. Xia, X. Zhang, Z. Meng, P. Bartocci, F. Fantozzi, Y. Chen, H. Chen, P. T. Williams, H. Yang, *ChemSusChem*, 2020, **13**, 938–944.
58 X. Yan, Y. Jia, K. Wang, Z. Jin, C.-L. Dong, Y.-C. Huang, J. Chen, X. Yao, *Carbon Energy*, 2020, **2**, 452-460.
59 K. Liu, G. Wu, G. Wang, *J. Phys. Chem. C*, 2017, **121**, 11319–11324.
60 M. Xiao, Z. Xing, Z. Jin, C. Liu, J. Ge, J. Zhu, Y. Wang, X. Zhao, Z. Chen, *Adv. Mater.*, 2020, **32**, 2004900.
61 J. Amaro-Gahete, A. M. Kaczmarek, D. Esquivel, C. Jiménez-Sanchidrián, P. Van Der Voort, F. J. Romero-Salguero, *Chem. – A Eur. J.*, 2019, **25**, 6823–6830.
62 M. Ruben, J. Rojo, F. J. Romero-Salguero, L. H. Uppadine, J.-M. Lehn, *Angew. Chem. Int. Ed.*, 2004, **43**, 3644–3662.
63 D. Esquivel, A. M. Kaczmarek, C. Jiménez-Sanchidrián, R. Van Deun, F. J. Romero-Salguero, P. Van Der Voort, *J. Mater. Chem. C*, 2015, **3**, 2909–2917.
64 A. M. Kaczmarek, D. Esquivel, J. Ouwehand, P. Van Der Voort, F. J. Romero-Salguero, R. Van Deun, *Dalton Trans.*, 2017, **46**, 7878–7887.
65 A. M. Kaczmarek, D. Esquivel, B. Laforce, L. Vincze, P. Van Der Voort, F. J. Romero-Salguero, R. Van Deun, *Luminescence*, 2018, **33**, 567–573.
66 A. Zuliani, M. Cano, F. Calsolaro, A. R Puente Santiago, J. J Giner-Casares, E. Rodríguez-Castellón, G. Berlier, G. Cravotto, K. Martina, R. Luque, *Sustain. Energy & Fuels*, 2021, **5**, 720-731.
67 X. Wang, J. Sunarso, Q. Lu, Z. Zhou, J. Dai, D. Guan, W. Zhou, Z. Shao, *Adv. Energy Mater.*, 2020, **10**, 1903271.
68 M. N. Roudbari, R. Ojani, J. B. Raoof, *Renew. Energy*, 2020, **159**, 1015–1028.
69 L. Huang, S. Zaman, X. Tian, Z. Wang, W. Fang, B. Y. Xia, *Acc. Chem. Res.*, 2021, **54**, 311–322.
70 A. Sobkowiak, D. Naróg, D. T. Sawyer, *J. Mol. Catal. A Chem.*, 2000, **159**, 247–256.
71 D. Naróg, A. Szczepanik, A. Sobkowiak, *Catal. Lett.*, 2008, **120**, 320–325.
72 M. Simón, A. Benítez, A. Caballero, J. Morales, O. Vargas, *Batteries*, 2018, **4**, 13.
73 A. Sayah, F. Habelhames, A. Bahloul, B. Nessark, Y. Bonnassieux, D. Tendelier, M. El Jouad, *J. Electroanal. Chem.*, 2018, **818**, 26–34.
74 J. Amaro-Gahete, A. Benítez, R. Otero, D. Esquivel, C. Jiménez-Sanchidrián, J. Morales, Á. Caballero, F. Romero-Salguero, *Nanomaterials*, 2019, **9**, 152.
75 A. Benítez, A. Caballero, J. Morales, J. Hassoun, E. Rodríguez-Castellón, J. Canales-Vázquez, *Nano Res.*, 2019, **12**, 759–766.
76 M. Matsumoto, Y. Saito, C. Park, T. Fukushima, T. Aida, *Nat. Chem.*, 2015, **7**, 730–736.
77 V. León, M. Quintana, M. A. Herrero, J. L. G. Fierro, A. D. La Hoz, M. Prato, E. Vázquez, *Chem. Commun.*, 2011, **47**, 10936–10938.
78 S. Alwarappan, S. Boyapalle, A. Kumar, C.-Z. Li, S. Mohapatra, *J. Phys. Chem. C*, 2012, **116**, 6556–6559.
79 J. Zhu, D. Yang, Z. Yin, Q. Yan, H. Zhang, *Small*, 2014, **10**, 3480–3498.
80 J.-C. Li, P.-X. Hou, C. Liu, *Small*, 2017, **13**, 1702002.

Please do not adjust margins

Please do not adjust margins

81 L. Gong, H. Zhang, Y. Wang, E. Luo, K. Li, L. Gao, Y. Wang, Z. Wu, Z. Jin, J. Ge, et al., *Angew. Chem. Int. Ed*., 2020, **132**, 14027–14032.
82 D. Lyu, Y. B. Mollamahale, S. Huang, P. Zhu, X. Zhang, Y. Du, S. Wang, M. Qing, Z. Q. Tian, P. K. Shen, *J. Catal*., 2018, **368**, 279–290.
83 J. Zhang, D. He, H. Su, X. Chen, M. Pan, S. Mu, *J. Mater. Chem. A*, 2014, **2**, 1242–1246.
84 Y. Chen, S. Xie, L. Li, J. Fan, Q. Li, Y. Min, Q. Xu, J. *Nanoparticle Res.*, 2021, **23**, 68.
85 F. J. Pérez-Alonso, M. A. Salam, T. Herranz, J. L. Gómez de la Fuente, S. A. Al-Thabaiti, S. N. Basahel, M. A. Peña, J. L. G. Fierro, S. Rojas, *J. Power Sources*, 2013, **240**, 494–502.
86 B. Ni, R. Chen, L. Wu, X. Xu, C. Shi, P. Sun, T. Chen, *ACS Appl. Mater. Interfaces*, 2020, **12**, 23995–24006.
87 K. R. Paton, E. Varrla, C. Backes, R. J. Smith, U. Khan, A. O'Neill, C. Boland, M. Lotya, O. M. Istrate, P. King, et al., *Nat. Mater*., 2014, **13**, 624–630.
88 A. Bianco, H.-M. Cheng, T. Enoki, Y. Gogotsi, R. H. Hurt, N. Koratkar, T. Kyotani, M. Monthioux, C. R. Park, J. M. D. Tascon, et al., *Carbon*, 2013, *65*, 1–6.
89 G.-L. Chai, K. Qiu, M. Qiao, M.-M. Titirici, C. Shang, Z. Guo, *Energy Environ. Sci*., 2017, **10**, 1186–1195.
90 X. Cheng, P. Yan, S. Liu, M. Qian, B. Wang, Z. Wan, J. Tian, X.-C. Shen, T. T. Isimjan, X. Yang, *Int. J. Hydrogen Energy*, 2019, **44**, 12127–12137.
91 U. I. Kramm, I. Abs-Wurmbach, I. Herrmann-Geppert, J. Radnik, S. Fiechter, P. Bogdanoff, *J. Electrochem. Soc*., 2011, **158**, B69.
92 Y. Li, G. Louarn, P.-H. Aubert, V. Alain-Rizzo, L. Galmiche, P. Audebert, F. Miomandre, *Carbon*, 2016, **105**, 510–520.
93 S. Biniak, G. Szymański, J. Siedlewski, A. Świątkowski, *Carbon*, 1997, **35**, 1799–1810.
94 S. Maldonado, S. Morin, K. J. Stevenson, *Carbon*, 2006, **44**, 1429–1437.
95 N. Zhang, T. Zhou, M. Chen, H. Feng, R. Yuan, C. Zhong, W. Yan, Y. Tian, X. Wu, W. Chu, et al., *Energy Environ. Sci*., 2020, **13**, 111–118.
96 M. Xiao, J. Zhu, L. Feng, C. Liu, W. Xing, *Adv. Mater*., 2015, **27**, 2521–2527.
97 G. Murdachaew, K. Laasonen, *J. Phys. Chem. C*, 2018, **122**, 25882–25892.
98 M. Mullet, V. Khare, C. Ruby, *Surf. Interface Anal*., 2008, **40**, 323–328.
99 H. Kong, J. Song, J. Jang, *Chem. Commun*., 2010, **46**, 6735.
100 Q. Zuo, P. Zhao, W. Luo, G. Cheng, *Nanoscale*, 2016, **8**, 14271–14277.
101 K. Zhu, C. Jin, Z. Klencsár, A. Ganeshraja, J. Wang, *Catalysts*, 2017, **7**, 138.
102 U. A. do Rêgo, T. Lopes, J. L. Bott-Neto, A. A. Tanaka, E. A. Ticianelli, *J. Electroanal. Chem*., 2018, **810**, 222–231.
103 Á. García, M. Retuerto, C. Dominguez, L. Pascual, P. Ferrer, D. Gianolio, A. Serrano, P. Assmann, D. G. Sanchez, M. A. Peña, et al., *Appl. Catal. B*, 2020, **264**, 118507.
104 B. J. Kim, D. U. Lee, J. Wu, D. Higgins, A. Yu, Z. Chen, *J. Phys. Chem. C*, 2013, **117**, 26501–26508.
105 Y.-L. Liu, X.-Y. Xu, C.-X. Shi, X.-W. Ye, P.-C. Sun, T.-H. Chen, *RSC Adv.*, 2017, **7**, 8879–8885.
106 J. Li, H. Zhang, W. Samarakoon, W. Shan, D. A. Cullen, S. Karakalos, M. Chen, D. Gu, K. L. More, G. Wang, et al., *Angew. Chem. Int. Ed*., 2019, **58**, 18971–18980.
107 L. P. Wijesinghe, S. D. Perera, E. Larkin, G. M. Ó Máille, R. Conway-Kenny, B. S. Lankage, L. Wang, S. M. Draper, *RSC Adv*., 2017, **7**, 24163–24167.
108 W. Li, C. Min, F. Tan, Z. Li, B. Zhang, R. Si, M, Xu, W. Liu, L. Zhou, Q. Wei, Y. Zhang, X. Yang, *ACS Nano*, 2019, **13**, 3, 3177–3187.
109 A. Bonakdarpour, T. R. Dahn, R. T. Atanasoski, M. K. Debe, J. R. Dahn, *Electrochem. Solid-State Lett.*, 2008, **11**, B208.
110 G. A. Ferrero, K. Preuss, A. Marinovic, A. B. Jorge, N. Mansor, D. J. L. Brett, A. B. Fuertes, M. Sevilla, M.-M. Titirici, *ACS Nano*, 2016, **10**, 5922–5932.
111 T. Kou, S. Wang, J. L. Hauser, M. Chen, S. R. J. Oliver, Y. Ye, J. Guo, Y. Li, *ACS Energy Lett*., 2019, **4**, 622–628.
112 C. Leal-Rodríguez, D. Rodríguez-Padrón, Z. A. Alothman, M. Cano, J. J. Giner-Casares, M. J. Muñoz-Batista, S. M. Osman, R. Luque, *Nanoscale*, 2020, **12**, 8477–8484.
113 M. E. G. Lyons, M. P. Brandon, *Int. J. Electrochem. Sci*., 2008, **3**, 41.
114 K. Lemoine, J. Lhoste, A. Hémon-Ribaud, N. Heidary, V. Maisonneuve, A. Guiet, N. Kornienko, *Chem. Sci*., 2019, **10**, 9209–9218
115 J. Zhao, M. Cano, J. J. Giner-Casares, R. Luque, G. Xu, *Energy Environ. Sci.*, 2020, **13**, 2618–2656.
116 Y. Gönüllü, K. Kelm, S. Mathur, B. Saruhan, *Chemosensors*, 2014, **2**, 69–84.
117 D. Alba-Molina, A. R. Puente Santiago, J. J. Giner-Casares, E. Rodríguez-Castellón, M. T. Martín-Romero, L. Camacho, R. Luque, M. Cano, *J. Mater. Chem. A*, 2019, **7**, 20425–20434.
118 D. Alba-Molina, A. R. Puente Santiago, J. J. Giner-Casares, M. T. Martín-Romero, L. Camacho, R. Luque, M. Cano, *J. Phys. Chem. C*, 2019, **123**, 9807–9812.

This journal is © The Royal Society of Chemistry 20xx

Please do not adjust margins